Stabilized ferroelectric NaNbO3 nanowires for lead-free piezoelectric nanocomposite applications

Minh-Thanh Do, Kévin Zimny, Abhishek Singh Dahiya, Jinkai Yuan, Rajaoarivelo Mbolotiana, Éric Lebraud, Cédric Lambin, François Lagugné-Labarthet, Wilfrid Neri, Mario Maglione, et al.

Stabilized Ferroelectric $NaNbO_3$ Nanowires for Lead-Free Piezoelectric Nanocomposite Applications

Minh-Thanh Do,[a] Kévin Zimny,[b] Abhishek Singh Dahiya,[b] Jinkai Yuan,[a] Rajaoarivelo Mbolotiana,[a] Eric Lebraud,[b] Cédric Lambin,[c] François Lagugné-Labarthet,[c] Wilfrid Neri,[a] Mario Maglione,[b] Annie Colin,[d] Marie-Hélène Delville,[b] Philippe Poulin,[a,]*

[a] Centre de Recherche Paul Pascal, University of Bordeaux, CNRS, Pessac 33600, France

[b] Univ. Bordeaux, CNRS, Bordeaux INP, ICMCB, UMR 5026, Pessac F-33608, France

[c] Western University, Department of Chemistry, 1151 Richmond Street, London, On, N6A 5B7, Canada

[d] MIE Team, Chimie Biologie Et Innovation, ESPCI Paris, PSL University, CNRS, 75005 Paris, France

*Corresponding authors: philippe.poulin@crpp.cnrs.fr

ABSTRACT: Ferroelectric nanomaterials often suffer from a severe polarization loss compared to their bulks due to a size-induced alteration in their crystalline structure, making them inefficient for piezoelectric applications. Discovering nanomaterials with efficient piezoelectric properties is therefore a challenging task. We report here a direct observation of a single-phase ferroelectric structure with stripe domains stabilized by size-induced thermal residual stress in $NaNbO_3$ nanowires (NWs) and demonstrate their excellent efficiency for lead-free piezoelectric nanocomposites. Polymer composites containing $NaNbO_3$ NWs exhibit piezoelectric coefficients and figure-of-merit values comparable to those of $KNbO_3$ NWs and approximately 9 and 100 times higher, respectively, than those of the reference devices using competing $BaTiO_3$ NWs. The remarkable performance of $NaNbO_3$ NWs compared to $BaTiO_3$ NWs contradicts the ranking of bulk properties claiming that $NaNbO_3$ ceramics are significantly less active than $BaTiO_3$. However, this counterintuitive behavior can be well understood if we consider structure modifications of these materials at the nanoscale, with a size-induced anti-ferroelectric to ferroelectric transition in $NaNbO_3$ NWs and ferroelectric to paraelectric transition in $BaTiO_3$ NWs. These findings are further supported by second harmonic generation characterizations, revealing substantially stronger second harmonic intensities for $NaNbO_3$ and $KNbO_3$ NWs compared to $BaTiO_3$ NWs. Our work confirms the critical role of structural properties in the macroscopic piezoelectric performances of nanomaterials, beyond the ranking of the bulk properties. With their scalable synthesis and high aspect ratio, ferroelectric $NaNbO_3$ NWs hold great promise for the large-scale production of efficient, lead-free piezoelectric nanocomposites.

KEYWORDS: Nanowires, $NaNbO_3$, piezoelectric properties, PVA, nanocomposites

INTRODUCTION

Ferroelectric nanomaterials are widely used in piezoelectric polymer composites, that have the potential to act as flexible electromechanical transducers, sensors, and generators.[1–3] Compared to bulk devices, nanocomposites can conform well to curved surfaces and withstand high-amplitude vibrations, making them potential candidates for harvesting energy from biomechanical sources. The piezoelectric nanocomposites also have a great potential for structural health monitoring in composite materials.

The macroscopic piezoelectric performance of nanocomposites critically depends on the intrinsic ferroelectric polarization of the included nanomaterials and the mechanical coupling between the nanomaterials and the polymer matrix. The mechanical coupling in polymer composites is typically weak because polymers are much softer than inorganic nanomaterials. This leads to ineffective stress transfer and low piezoelectric activity of the nanomaterials when the composites are subjected to mechanical stress. To resolve this problem, nanomaterials with an anisotropic shape and high aspect ratio, such as nanowires (NWs), can be used instead of nanoparticles (NPs).[4–9] According to the shear-lag model,[10,11] stress transfer is substantially improved for anisotropic particles with a high aspect ratio. However, the piezoelectric functionality is only significant if the embedded NWs possess a decent intrinsic microscopic ferroelectric polarization which is directly influenced by the size and crystalline structure of the NWs. Compared to bulk ceramics, nanomaterials may suffer from a strong ferroelectric polarization depression due to alterations in their crystalline structures at the nanoscale.[12–14] Therefore, piezoelectric devices may show limited functional performance even using nanomaterials that display excellent bulk properties.

$BaTiO_3$ (BTO) is the most common lead-free piezoelectric ceramic, with a piezoelectric coefficient $d_{33} \approx 300$ pC/N, significantly higher than 100 pC/N of $KNbO_3$ (KNO) and 30 pC/N of $NaNbO_3$ (NNO), see **Figure S1** in the Supporting Information (SI) with references therein. However, BTO NPs suffer from severe polarization loss due to a transition from tetragonal to cubic structure.[14] In contrast to BTO, $NaNbO_3$ (NNO) nanomaterials show an interesting ferroelectric phase increment with decreasing size.[15,16] NNO NPs stabilize in a ferroelectric (FE) phase with a non-centrosymmetric structure in the space group $P2_1ma$ (alternative $Pmc2_1$, no. 26) while bulky particles and ceramics are mainly in an anti-ferroelectric (AFE) phase with a centrosymmetric structure in the space group Pbma (alternative Pbcm, no. 57).[15,16] These findings can pave the way for lead-free piezoelectric applications of NNO nanomaterials. NNO NWs have been successfully synthesized at the gram scale by hydrothermal methods.[17,18] With a very high aspect ratio (a length up to hundreds of μm and a diameter of ≈ 100 nm),[18] NNO NWs are expected to exhibit efficient mechanical coupling with polymer matrices in nanocomposites. However, the crystalline structures and microscopic ferroelectric properties of NNO NWs, which are crucial for piezoelectric performances, remain unclear. Indeed, Ke *et al.*[18] and David *et al.*[19] reported NNO NWs with an AFE phase, while Jung *et al.*[20] and Ji *et al.*[21] mentioned NNO NWs with an FE phase. The latter groups, however, found opposite FE and AFE phases in hydrothermal NNO NPs, the siblings of hydrothermal NNO NWs, obtained at a longer reaction time. Therefore, the accurate study of the structural properties of NNO nanomaterials, in particular the high aspect-ratio NNO NWs, calls critically for further research. Moreover, there is high demand for a fair comparison between the different ferroelectric NWs to determine the most practical ones for piezoelectric applications. This task cannot yet be performed based on the available literature because of the many differences in filler contents, polymer matrices, device dimensions, and test conditions.

In this work, we report a direct observation of the size-induced single-phase ferroelectric structure with stripe domain patterns in NNO NWs and prove that these NNO NWs are superior for piezoelectric applications compared to BTO NWs. NNO NW-based polymer composites show piezoelectric coefficient and figure-of-merit which are respectively about 9 and 100 times higher than those of the BTO NW-based composites and are competitive to those of KNO NW-based composites. The superior piezoelectric performance of NNO NWs results directly from the non-centrosymmetric structure of the ferroelectric phase, which cannot be achieved entirely in NNO bulk ceramics. In contrast, BTO NWs, the most common lead-free piezoelectric materials, are much less efficient due to a destabilization of the tetragonal structure at the nanoscale. The present results are supported by X-ray diffractions (XRD), high-resolution transmission electron microscopy (HR-TEM), and second harmonic generation (SHG) experiments. Our work confirms the critical role of the microscopic ferroelectricity in the macroscopic piezoelectricity of these nanomaterials, beyond the ranking of the bulk properties. These NNO NWs obtained by simple, scalable synthesis exhibit an anisotropic morphology with a decent microscopic ferroelectric structure; this makes them highly promising for lead-free piezoelectric nanocomposite applications.

RESULTS AND DISCUSSION

NNO NWs were obtained by annealing hydrothermal $Na_2Nb_2O_6.H_2O$ NW templates (see the experimental section for more details). The $Na_2Nb_2O_6.H_2O$ NWs can only be obtained within a narrow synthesis window, otherwise, they transform into NNO NPs[17,18] unless we use silicone oil as a surfactant to significantly expand the synthesis conditions .[22] An amount of 1.4 g of NNO NWs can be achieved per synthesis (**Figure 1a**). The NNO NWs have a length of up to hundreds of µm

and a diameter of about 80 - 130 nm, as shown by scanning electron microscopy (SEM) images in **Figure 1b**. This diameter range is well consistent with typical values ranging from 60 to 200 nm of previously reported NNO NWs.[17–22] The diameter variation may be attributed to different synthesis conditions (such as precursor concentration, reaction time, temperature, and the presence of silicone oil) and the non-cylindrical cross-sectional shape of the NWs. For comparison, NNO NPs, synthesized in a longer hydrothermal reaction without surfactant, are presented in **Figure 1c**. A detailed mechanism behind the facilitated formation of $Na_2Nb_2O_6.H_2O$ NWs by silicone oil has been proposed in the original study.[22] Essentially, silicone oil molecules attach to the surface of the $Na_2Nb_2O_6.H_2O$ NWs, subsequently weaken the attack of OH^- on the $Na_2Nb_2O_6.H_2O$ metastable structures and kinetically slow down the dissolution of $Na_2Nb_2O_6.H_2O$ NWs and the formation of $NaNbO_3$ NPs. The synthesis conditions for $Na_2Nb_2O_6.H_2O$ NWs are therefore significantly expanded, in terms of both reaction temperature and time.

The AFE phase (space group Pbma) and FE phase (space group $P2_1ma$) of NNO are distinguished by the displacement of the Nb ions and the tilting of the octahedral oxygens (**Figure 1d)**. The AFE phase follows the Glazer $[a^-b^+a^-/a^-b^-a^-]$ tilting system and has bulk lattice parameters of a = 5.556 Å, b = 15.520 Å, c = 5.506 Å, while the FE phase follows the $[a^-b^+a^-]$ tilting system with a = 5.582 Å, b = 7.782 Å, c = 5.528 Å.[23] The AFE and FE phases have their b-axis parameters formed by quadrupling and doubling, respectively, the lattice parameter of the standard perovskite structure. They, thus, exhibit distinguished superstructure diffractions. The overall X-ray diffraction (XRD) patterns of NNO NWs and NNO NPs are quite similar, as shown in **Figure 1e).** However, the enlarged patterns at 2θ = 35.5 – 37.5°, 42.5 – 44.0°, 54.5 – 56.0°, and 59.5 – 61.5° show clearly that NNO NWs present the characteristic diffraction peaks of the FE phase (ICSD 98-007-4642) while NNO NPs exhibit mainly the diffraction peaks of the AFE phase

(ICSD 98-002-3239) (**Figure 1f)**. There is no diffraction signal of the AFE phase in the patterns of the NNO NWs. The phase difference between the NNO NWs and the NNO NPs is also observed by Raman spectroscopy (**Figure S2**). These data support the conclusion that the NNO NWs are stabilized in the FE phase while the NNO NPs are stabilized in the AFE phase.[21]

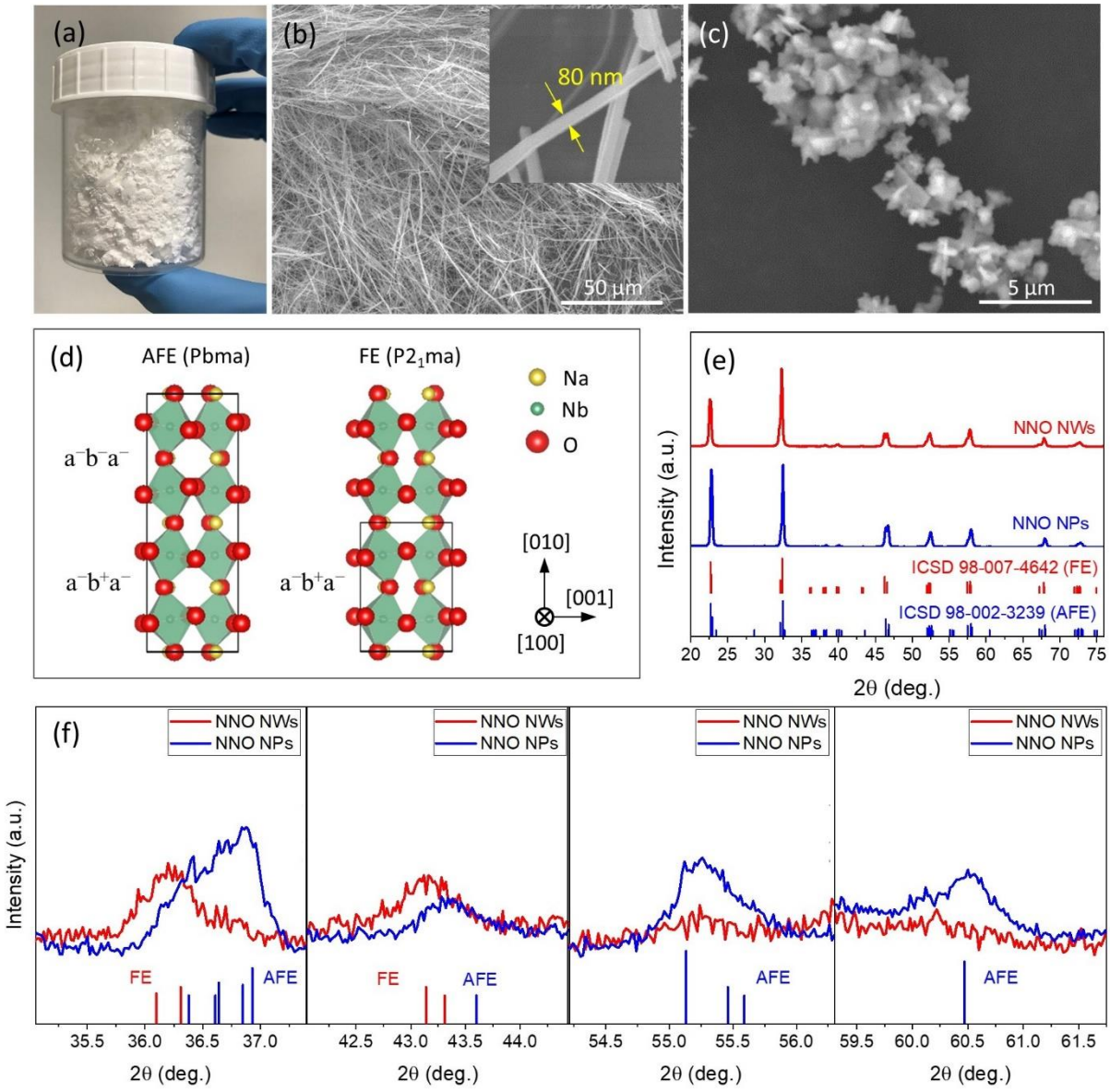

Figure 1. (a) Photograph of 1.4 g of NNO NWs obtained from a single synthesis. SEM images of (b) NNO NWs and (c) NNO NPs. (d) Schematic crystal structures of NNO AFE and FE phase. (e)

Overall and (f) enlarged XRD patterns of NNO NWs and NNO NPs compared with the standard diffractions of the NNO FE phase (ICSD 98-007-4642) and AFE phase (ICSD 98-002-3239).

The crystalline structures of NNO nanomaterials are further characterized by high-resolution transmission electron microscopy (HR-TEM) and selected area electron diffractions (SAED), as shown in **Figure 2**. Both NNO NWs and NNO NPs exhibit a single-crystal nature as their SAED pattern along different axes shows clear individual reflection dots. For NNO NPs, their SAED patterns taken along [100] and [101] zone axes show a pattern of quarter-integral superstructure reflections, denoted by yellow rectangles in **Figure 2b*, c***, which is a characteristic nature of the AFE phase. On the other hand, the SAED patterns of NNO NWs taken along [100] and [101] zone axes, show clear characteristic half-integral superstructure reflections of the FE phase (**Figure 2d*, e***). These data strongly confirm the FE structure of the NNO NWs and the AFE structure of the NNO NPs. More importantly, one can clearly observe stripe patterns on the NNO NWs as shown in **Figure 2e, f**. The stripe patterns in NNO NWs look similar to those observed in the FE regions of bulk NNO ceramics.[24] The formation of stripe domains is typical of FE materials ensuring their structures achieve an energetically favorable state. We, therefore, believe that these stripe patterns represent the FE domains within the NNO NWs even though their widths, approximately several nanometers, are much smaller than the typical width of FE domains in thin films and bulk ceramics, which is of the order of tens or hundreds of nanometers. Further characterizations by higher resolution TEM would be particularly interesting to more clearly describe the FE domains and/or structural defects inside the NNO NWs.

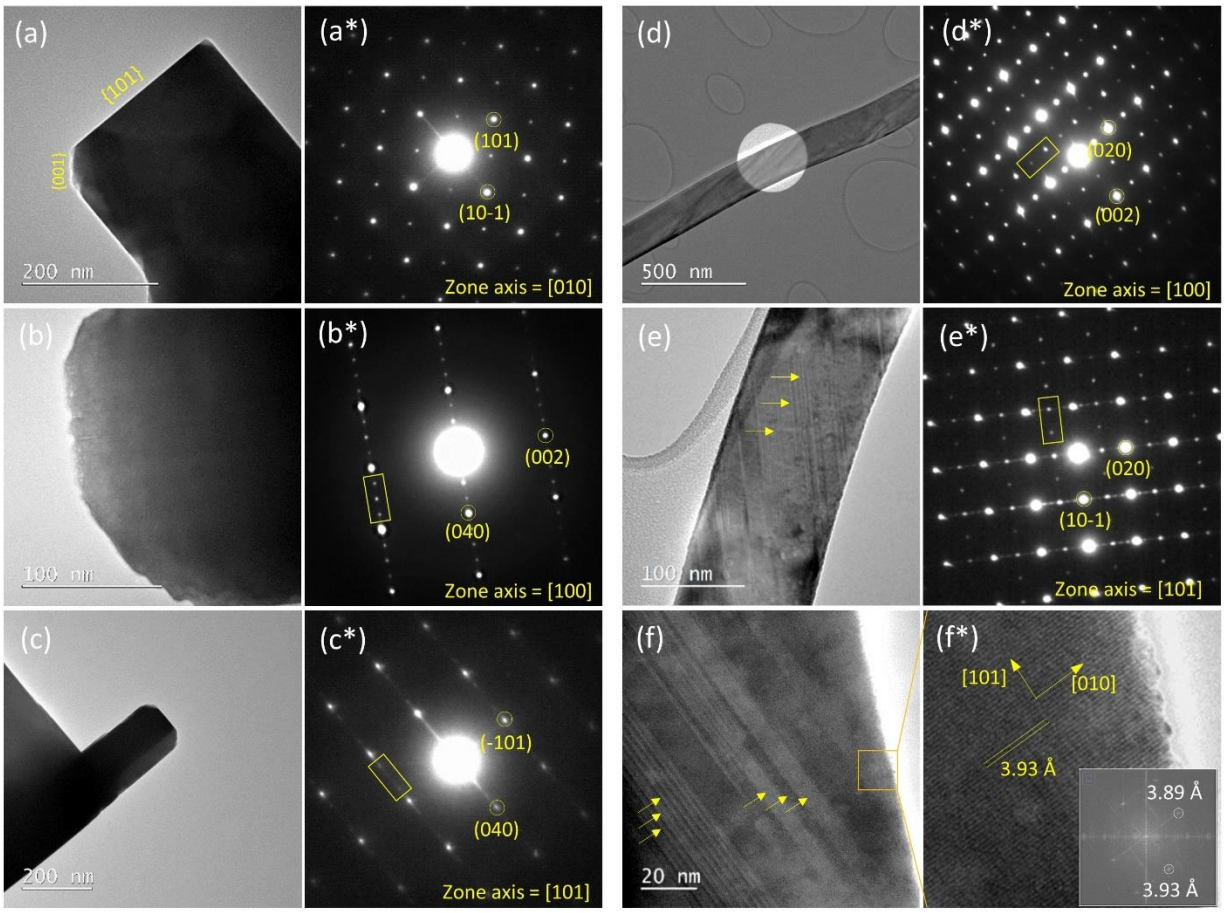

Figure 2. TEM and SAED characterizations of NNO NPs (a-c*) and NNO NWs (d-f*). The yellow rectangles in SAED patterns (b*-e*) denote the characteristic superstructure reflections of the AFE phase in NNO NPs and the FE phase in NNO NWs, respectively. The arrows in TEM images (e-f) denote the stripe patterns of FE domains in NNO NWs. The inset in (f*) shows the Fast Fourier Transform of the corresponding structure of the NNO NWs.

Our structural characterizations reveal that NNO NWs stabilize in the FE phase, similar to NNO NPs synthesized by microemulsion-mediated and solid-state synthesis,[15,16] while hydrothermal NNO NPs stabilize in the AFE phase, similar to typical NNO bulk samples. These different phase stabilizations can be attributed to different scales of residual stress inside the

nanomaterials synthesized by different methods. Hydrothermal NNO particles crystallize within a solution medium at a temperature typically below 200 ºC, thus experience a negligible internal stress and exhibit a distinct cuboid shape with well-defined crystal planes on the surface. As a consequence, the hydrothermal NNO NPs in this study and NNO micro-size particles in a previous study,[21] consistently exhibit a single AFE phase, which is more energetically favorable than the FE phase. In contrast, the NNO particles made by the other two methods require prolonged calcination at high temperatures (≥ 400 ºC) to reach crystallinity and then manifest an irregular shape with undefined surfaces.[15,16] It is worth noting that NNO NWs crystallize from $Na_2Nb_2O_6.H_2O$ NW templates during annealing at 600 °C. The crystallization under confinement conditions can result in a significant thermal residual stress present in these NNO NPs and NWs as they cool to room temperature, which can stabilize the energetically unfavorable non-centrosymmetric FE phase. Indeed, calcined crystalline NNO particles only show the FE phase if the particle size falls below the sub-micro scale while the larger particles remain in the AFE phase.[15] Moreover, the FE phase is observed in NNO bulk ceramics with nano-size grains, and the fraction of the FE phase increases with decreasing grain size.[25] All of these observations are understandable as the thermal residual stress only becomes pronounced in NPs and nano-grains. The bulky particles and grains may contain many structural defects which can easily release the thermal residual stress during the cooling of the material, resulting in a stable AFE phase. In addition, compressive epitaxial stressed NNO thin films are observed to be stable in an FE phase.[26–28] All of these findings support the hypothesis that internal compressive stress (whether from thermal residual stress and/or from epitaxial stress) stabilizes the FE phase in NNO nanomaterials.

We suspect that NNO nanowires with bigger diameters will display, at some point, a transition toward an AFE phase similar to NNO bulk materials. The exact size range of this

transition is still unknown and would be a topic for interesting future research. More intriguingly, much thinner NWs might display better properties, in terms of polarization and piezoelectric activity, even if the presently investigated NWs are already in a stable FE phase. Again, the diameter dependence of crystalline structure and functional properties of NNO NWs deserves future research.

To characterize the piezoelectric properties of the nanomaterials, we embedded them in a polyvinyl alcohol (PVA) matrix and measured the macroscopic piezoelectric constant d_{33} of the composites. This method directly evaluates the practical application of the nanomaterials and avoids the artifacts present in piezoelectric force microscopy methods performed on individual NWs.[29] In addition, the PFM signal is highly sensitive to the analyzed position and orientation of the nanomaterial specimens, posing a challenge for a fair comparison between different samples. We also characterized the piezoelectric activity of hydrothermal $BaTiO_3$ (BTO) NWs[30,31] and $KNbO_3$ (KNO) NWs[32] for a comparison between these common lead-free NWs. The BTO NWs have a diameter of 200 - 300 nm and a length of 3 - 5 µm and crystallize in a tetragonal structure but approaching the cubic one (**Figure S3**). The KNO NWs crystallize in a monoclinic structure with a length of 2 - 4 µm and a diameter of 110 - 130 nm (**Figure S4**), which are well consistent with data in the previous study.[32] Besides these hydrothermal NWs, we also tested commercial BTO NPs of 100 nm size (BTO100) and 500 nm size (BTO500) as references. Hydrothermal NNO NPs are excluded from consideration as they show poor piezoelectricity compared to NNO NWs.[20,21]

The PVA/nanomaterial composites were formulated by a water-based solution casting method, see Methods section. The composites of 50 wt% nanomaterials are flexible and can easily withstand strong mechanical torsion (**Figure 3a**). The composites have a high Young's modulus

of the order of GPa, which allows for an efficient stress transfer in the devices. These advantages come from the excellent mechanical properties of the PVA matrix and the homogeneous dispersion of the nanomaterials within this matrix (**Figure 3b-f)**. Due to stirring and sonication during the composite preparation, the as-prepared long NNO NWs are mechanically fractured once inside the composite. However, with a final length of 5-10 µm, their aspect ratios are still as high as 100, leading to good mechanical coupling with the polymer. The SEM cross-sectional images also show that the embedded NWs align horizontally along the main plane of the composite film. This behavior is attributed to the shear forces applying to the NWs during solution casting and water evaporation.

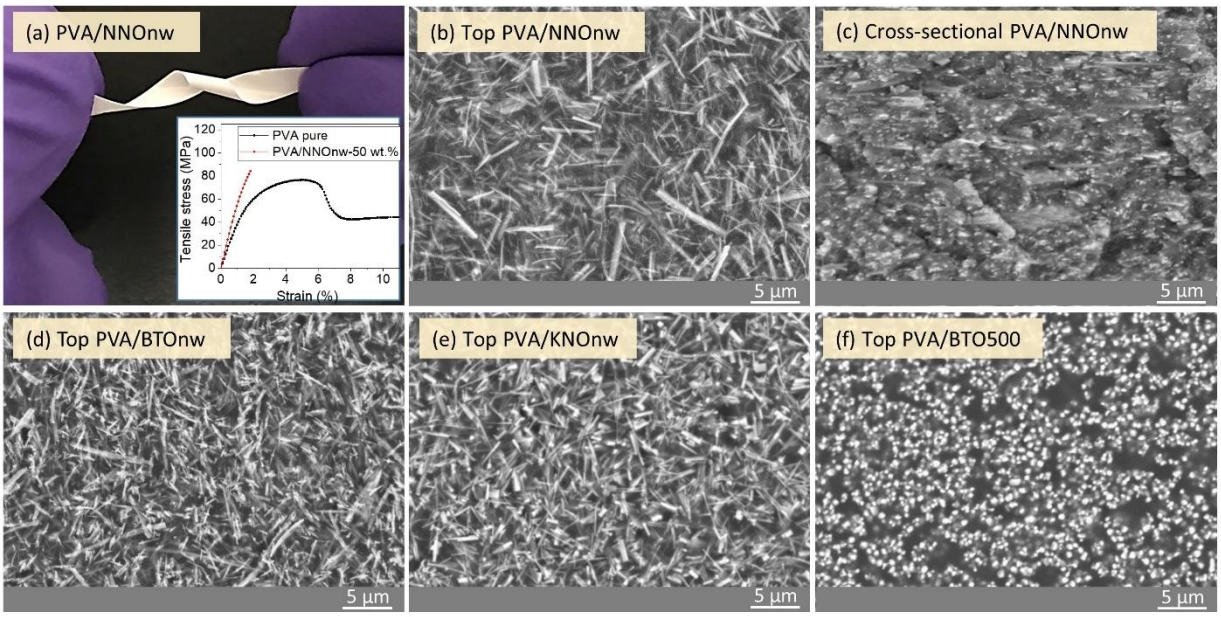

Figure 3. (a) Photograph of a PVA/NNOnw-50 wt.% lamella under mechanical twisting. The inset shows the stress-strain curves of a pure PVA film and the PVA/NNOnw-50 wt.% composite. (b-f) SEM images of the PVA composites with different nanomaterials. All the composites contain 50 wt% of nanomaterials.

Macroscopic piezoelectric coefficients, d_{33}, are measured after a prerequisite electrical poling is applied through the parallel Au electrodes on both sides of the samples. It is generally difficult to polarize ferroelectric nanomaterials embedded in polymer matrices because of a large dielectric mismatch between the two materials (dielectric constant of about 200-5000 for ferroelectrics but only of about 2-10 for polymers). However, the poling efficiency can be improved by operating at high temperatures. This is because (i) the polarization switching of the ferroelectric domains becomes easier at higher temperatures and, more importantly, (ii) the conductivity of the polymer increases with increasing temperatures, resulting in a higher local poling field inside the ferroelectric fillers.[33,34] Here, PVA/BTO500 composites were used as model samples to optimize the poling temperature. The PVA matrix contains ionic impurities left over from the polymer processing.[35] Its conductivity therefore dramatically increases with increasing temperature due to the increased mobility of these ions (**Figure S5**). As expected, the piezoelectric coefficient d_{33} of the composite increases with increasing poling temperature before reaching a maximum value at poling temperatures within 100 - 120 °C (**Figure 4a**). The poling efficiency of the BTO500 NPs is confirmed by the relative intensity of the (002) and (200) XRD peaks of the non-poled and poled composites (**Figure 4b**). The non-poled composite with randomly oriented BTO dipoles shows an intensity ratio of $(I_{(002)}/I_{(200)}) \approx 0.5$ because the number of (200) planes is twice that of the (002) planes. The composite poled under 50 kV/cm at room temperature also shows an $I_{(002)}/I_{(200)} \approx 0.5$, implying that only the 180°-switching of BTO dipoles is activated under this poling condition. A poling field of 100 kV/cm at room temperature is sufficient to activate the 90°-switching of BTO dipoles to some extent as the $I_{(002)}/I_{(200)}$ increases to ≈ 0.8. The switching of BTO dipoles becomes significantly efficient only when the poling of 50 kV/cm is performed at 100 °C, with an $I_{(002)}/I_{(200)}$ ≈ 2.9.

We then fixed the optimized poling temperature at 100 °C and varied the poling field to obtain the most efficient poling state and maximum achievable piezoelectric functions for each kind of nanocomposite. The piezoelectric coefficient d_{33} increases with the poling field before reaching a maximum plateau for all the composites (**Figure 4c**). This is a universal behavior of piezoelectric materials because ferroelectric dipoles can be better aligned at higher fields until they reach the maximum possible alignment state. However, NNO NWs and KNO NWs require a poling field of more than 100 kV/cm to fully activate their piezoelectricity, while BTO nanomaterials need only 25-50 kV/cm.[36] This difference can be correlated to the larger coercive fields of KNO and NNO ceramics, approximately 10-15 kV/cm[37–40] and 30-40 kV/cm,[41,42] respectively, compared to 2-5 kV/cm for BTO ceramics.[43,44] More importantly, the PVA/NNOnw-50 wt.% and PVA/KNOnw-50 wt.% composites show maximum values of d_{33} = 3.7 ± 0.2 and 3.4 ± 0.3 pC/N, approximately 9 times higher than the d_{33} = 0.4 ± 0.1 pC/N of the PVA/BTOnw-50 wt.% composite (**Figure 4d**). The PVA/BTO100-50wt.% shows a d_{33} = 0.9 ± 0.1 while the PVA/BTO500-50wt.% shows 2.8 ± 0.2 pC/N. The PVA/BTO500 composite outperforms previous composites combining tetragonal BTO NPs with polyurethane[36] and polyamide 11[45](**Table S1**). This improvement is attributed to the higher Young's modulus of PVA compared to other polymers, allowing for a more efficient stress transfer to the BTO NPs. The NNO NWs and KNO NWs also consistently exhibit a superior piezoelectric figure-of-merit (FOM) = $d_{33}^2/(\varepsilon.\varepsilon_0)$ compared to BTO NWs (**Figure 4e**), where ε and ε_0 are the dielectric constant of the composite and the vacuum, respectively. (**Figure S6**). The piezoelectric FOM of PVA/NNOnw-50 wt.% is about 100 times higher than that of the PVA/BTOnw-50wt.%. All the composites show a dielectric loss of less than 1 across the frequency range from 10^{-1} to 10^6 Hz (**Figure S6**), enabling them to be efficient for practical piezoelectric applications. All these data clearly indicate that NNO NWs are much more efficient for piezoelectric applications than BTO NWs.

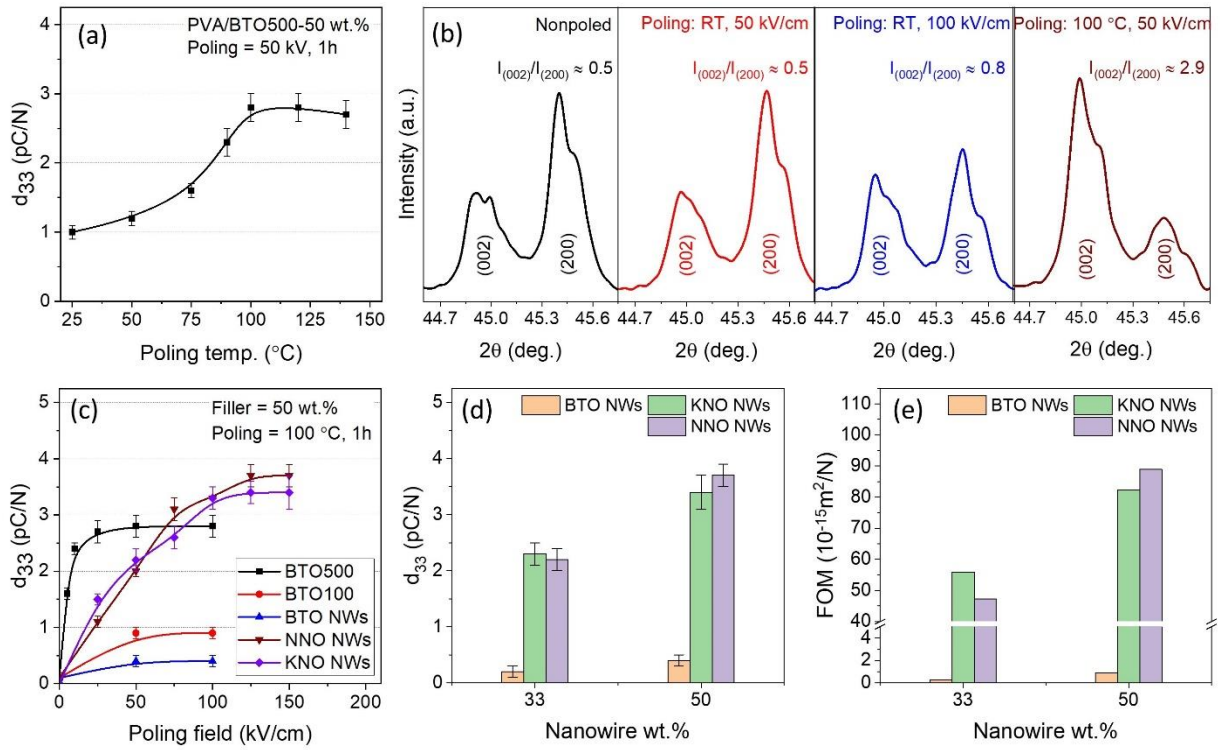

Figure 4. (a) Piezoelectric constant d_{33} of the PVA/BTO500-50 wt.% composite poled at various temperatures. (b) Enlarged XRD patterns of the PVA/BTO500-50% composite showing the BTO (002) and (200) peaks under different poling conditions. (c) Piezoelectric constant d_{33} of different composites as a function of the poling field. (d) Maximum piezoelectric constant d_{33} and (e) piezoelectric FOM of the composites with different NW contents.

The finding that NNO NWs are much more efficient than BTO NWs for piezoelectric applications contradicts the ranking of the bulk performances in which BTO ceramics ($d_{33} \approx 300$ pC/N) outperform NNO ceramics ($d_{33} \approx 30$ pC/N). However, these performance rankings can be understood by considering the structural properties of the materials in the bulk and at the nanoscale. In bulk NNO ceramics, the stable AFE with a centrosymmetric structure phase is inactive for piezoelectricity.[16,46] Although the AFE phase can transform into the non-centrosymmetric piezoelectric-active FE phase under strong electrical poling, the remaining AFE phase is still up to

50%.[46] This results in poor piezoelectricity of the NNO ceramics compared to the pure piezoelectric active tetragonal BTO ceramics. However, in NNO NWs, only the non-centrosymmetric structure FE phase is present, favoring a high piezoelectric performance, competitive with that of monoclinic KNO NWs. As far as BTO NWs are concerned, they show a destabilized tetragonal structure, close to a paraelectric cubic one, resulting in an inefficient piezoelectric performance (**Figure S3**). Hydrothermal BTO NWs have been widely used for piezoelectric nanocomposites. These previous works often concluded that BTO NWs had a tetragonal structure based on Raman characterizations.[47,48] However, the XRD patterns of these BTO NWs showed only one single diffracted peak at $2\theta \approx 45.2°$, indicating a weak tetragonal behavior of the material.[31,47–49] By studying the change in their (002)/(200) XRD peaks measured at room temperature and 150 °C, we prove here that the BTO NWs show an even weaker tetragonal behavior than 100 nm size BTO NPs (**Figure S3e**). This structural property consequently results in the limited piezoelectric performance of BTO NWs, even lower than that of commercial BTO NPs.

It is noted that we have studied and compared different NWs synthesized using commonly reported conditions in the literature, even if their diameter and length differ. The objective is to understand and explain differences in their physical properties originating from structural differences of these NWs. A definite comparison between NNO NWs and BTO NWs would require single-crystalline BTO NWs, which we could not achieve. We, however, point out that single-crystalline NNO NWs stabilize in a ferroelectric state while BTO nanomaterials always show decreased ferroelectricity. The single-crystalline BTO NWs reported in the literature appear to exhibit a low tetragonality, as indicated by a sharp single XRD (002)/(200) peak at $\approx 45.2°$.[48,49] This behavior is similar to that of our polycrystalline structures BTO NWs. Therefore, we believe that the piezoelectric performance of single-crystalline BTO NWs is also much lower than that of

ferroelectric NNO and KNO NWs. Although the piezoelectric functions are competitive among NNO NWs and KNO NWs, the NNO NWs would be more applicable from a practical point of view due to their high yield and easy scale-up synthesis, allowing large-scale production of devices. In addition, the ultimate length of the NNO NWs in the composites can also increase further with optimized composite processing (avoid prolonged sonication steps), facilitating an effective stress transfer within the composites. In this study, the piezoelectric functions are measured across the composite thickness, thus the role of the NW aspect ratio and alignment is minor compared to the crystalline structure. The piezoelectric performance of the NNO NW-based composites is found to be considerably enhanced when measured along the film plane, as opposed to the cross-sectional direction. This enhancement can be attributed to superior stress transfer from the polymer to the NWs along the main axis of the NWs lying within the film plane. A separate study will provide detailed findings on this aspect. Once again, in this study, we focus solely on the FE structure that enables NNO NWs to function efficiently as piezoelectric nanomaterials.

Non-centrosymmetric structures are expected to be active for second harmonic generation (SHG). Therefore, a series of polarized second harmonic measurements were performed under a microscope to record the SHG and polarization patterns of a single unpoled NW embedded in PVA (**Figure 5**). The SHG setup is described in the Method section. Briefly, an 800-nm fundamental beam from a 120-fs laser was focused onto a single NW with a set polarization, and the second harmonic photons were detected at 400 nm in the two orthogonal directions X and Y. In **Figure 5a-c**, the maps are collected with a horizontal (X) input polarization for the NWs oriented along the horizontal (X) direction. The collected signal is the sum of the polarized horizontal (X) and vertical (Y) signals detected by two separate avalanche photodiodes. All the NWs types show an SHG activity and for similar excitation parameters, the SHG intensities vary with $I_{SHG}(NNO) \sim$

$2\times I_{SHG}(KNO) \sim 9\times I_{SHG}(BTO)$. The experiments performed at several positions and over several NWs show that NNO NWs display the highest SHG intensity whereas the BTO ones show the weakest SHG response. The SHG signal is not homogenous over the entire length of the NWs, presumably due to local defects such as local crystalline orientation mismatch or possible tilted NWs with respect to the substrate plane. This lack of homogeneity is more pronounced in the case of BTO NWs that concomitantly show the presence of multiple crystallites along the NW (**Figure S3b)**) with possible different crystalline orientations, thus impacting the SHG polarized response and the signal intensity.

The polar plots in **Figure 5d-f** are obtained on selected points over the NWs (indicated by stars (★) in **Figure 5a-c** by rotating the input polarization over a full period and detecting the responses along the X and Y directions. The detailed analysis and fit of these SHG polar plots using the effective susceptibility tensors for each crystalline lattice is beyond the scope of this manuscript. The difference in the intensities and polarization patterns of the NWs is due to the different crystalline space groups and the corresponding independent and non-vanishing second-order susceptibility elements to be considered for the orthorhombic (mm2 symmetry class for NNO, 7 $\chi_{ijk}^{(2)}$ elements), monoclinic (m symmetry class for KNO, 14 $\chi_{ijk}^{(2)}$ elements) and tetragonal lattice (4mm symmetry class for BTO, 4 $\chi_{ijk}^{(2)}$ elements).[50] Interestingly, all NWs show an intense 2-lobe polarization response (**Figure 5d-f**, red polar plots) with a maximum obtained when both the input polarization and the analyzer are parallel and along the X direction, thus matching the orientation of the NWs oriented along X. The polarized response orthogonal to the wire directions (**Figure 5d-f**, blue polar plots) is weaker and shows a 4-lobe polar response. These data imply that the SHG intensity along the X direction is presumably driven by a dominant susceptibility tensor element while the intensity along the Y direction is driven by several susceptibility tensor elements

of comparable magnitude. The full SHG tensorial analysis of these polar plots would provide the local orientation of the crystallographic axes at the single NW level and possibly reveal the local defects with distinct crystallographic orientations or the presence of anti-ferroelectric domains.[51,52]

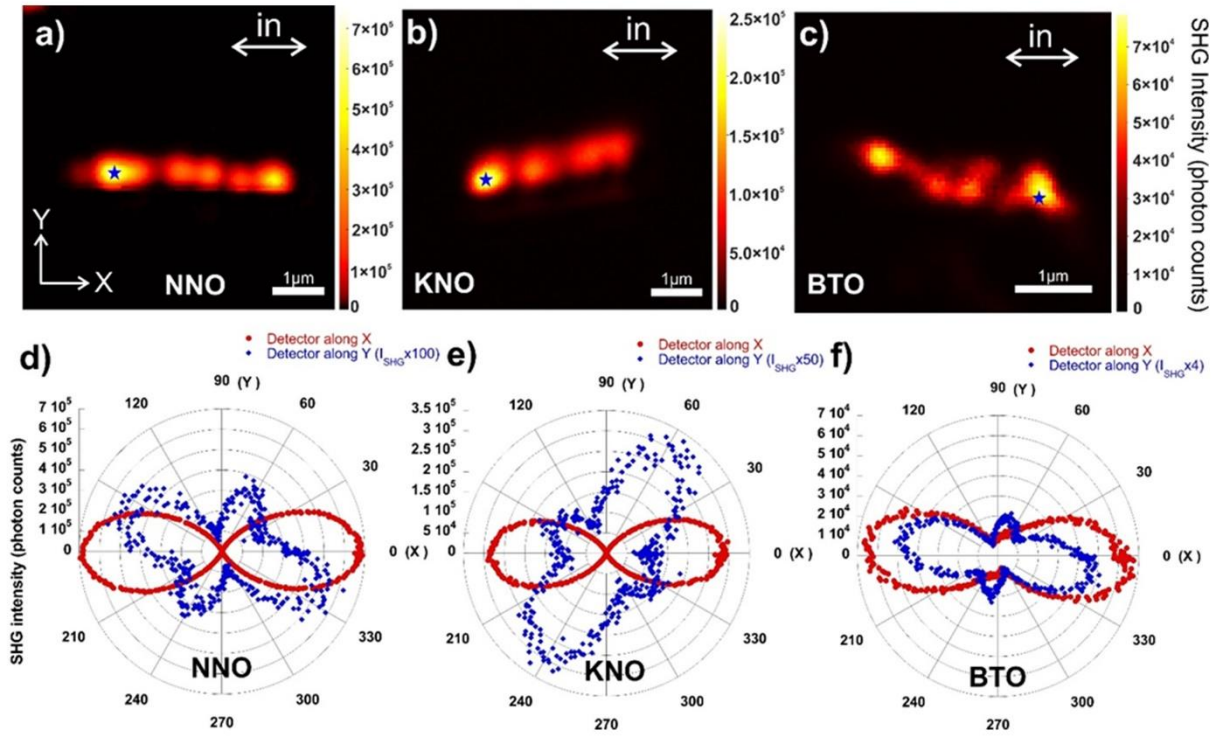

Figure 5. SHG maps with horizontal excitation of NNO (a), KNO (b), and BTO (c) NWs. The intensity is the sum of the X and Y polarized channels. Polar SHG response for a rotating input polarization over a 360° period for NNO (d), KNO (e), and BTO (f) on the selected spots indicated in the corresponding maps in (a-c). The polar plot in red is the SHG collected along the X-polarized channel while the blue polar plot is collected along the Y channel. At each selected spot over the wires, the intensities of the Y channel have been multiplied by 100 (NNO), 50 (KNO), and 4 (BTO) for better visualization.

CONCLUSIONS

In conclusion, we have reported a single ferroelectric phase, residual-stress-induced non-centrosymmetric orthorhombic structure with stripe domain patterns in hydrothermally-prepared $NaNbO_3$ NWs. These structural properties provide $NaNbO_3$ NWs with superior piezoelectric performances compared to rival $BaTiO_3$ nanomaterials, which suffer from severe ferroelectric loss due to a tetragonal-cubic transition at the nanoscale. Polymer composites of $NaNbO_3$ NWs exhibit a piezoelectric coefficient and a figure-of-merit that are respectively approximately 9 and 100 times higher than those of the $BaTiO_3$ NWs reference composites. The piezoelectric functions of $NaNbO_3$ NWs are competitive to those of monoclinic $KNbO_3$ NWs. The structural and piezoelectric results are further supported by a significantly higher second harmonic signal generated from $NaNbO_3$ and $KNbO_3$ NWs than from $BaTiO_3$ NWs. All these results confirm the critical importance of microscopic ferroelectric properties of nanomaterials for the macroscopic piezoelectric performance, beyond the ranking of bulk properties. Compared to $KNbO_3$ NWs, $NaNbO_3$ NWs with a very high aspect ratio can be synthesized simply on a large scale by hydrothermal method, and appear to be particularly promising for the mass production of efficient flexible piezoelectric composites. In addition, we also demonstrate that the PVA matrix is promising for polymer nanocomposites thanks to its excellent mechanical strength, enabling an efficient stress transfer from external mechanical impacts to embedded piezoelectric nanomaterials.

MATERIALS AND METHODS

General. NaOH, KOH, $Ba(OH)_2$, HCl, and PVA pellets (Mowiol(R) 20-98, 125000) were purchased from Aldrich. 100 and 500 nm BTO NPs were purchased from US Research Nanomaterials and Nb powder (99.8%) from Alfa Aesar. TiO_2 P25 was a generous gift from Evonik Company. Silicone oil G21V200 was from Rhodia (Solvay). The solvents were purchased from Aldrich. Chemicals were used without further purification.

Nanowire synthesis. NNO NWs were synthesized by a hydrothermal reaction combined with a post-calcination.[22] First, 0.80 g of Nb powder was dispersed into 120 ml of NaOH 10 M solution. The mixture was stirred for 1h and then 1.0 ml of silicone oil was added to the mixture. The mixture was then transferred into a 200-ml Teflon-lined stainless steel autoclave and maintained at 180 °C for 5h under 600 rpm stirring. The white product, known as $Na_2Nb_2O_6.H_2O$ NWs, was collected and washed carefully. These $Na_2Nb_2O_6.H_2O$ NWs were then annealed at 600 °C for 4h in the air to obtain the desired NNO NWs, approximately 1.4 g per synthesis. NNO NPs were synthesized following a similar procedure but with a hydrothermal reaction of 24 h without using the CS200 oil.

BTO NWs were synthesized based on a two-step hydrothermal procedure adapted from previous works.[30,31] In the first step, 1.76 g of TiO_2 P25 (0.63M) dispersed in 35 ml of NaOH 10 M solution (with 1h of Ar or N_2 purging before adding powders) was transferred into a 50-ml Teflon-lined stainless steel autoclave and stirred at room temperature for 1h. The autoclave was then introduced to a pre-heated oven at 200 °C for 72h. The collected precipitates known as $Na_2Ti_3O_7$ NWs, were washed with diluted HCl (0.1 M), DI water, and ethanol until the pH reached 7. In the second step,

0.10 g of $Na_2Ti_3O_7$ NWs were dispersed in 30 ml of $Ba(OH)_2$ 0.065M solution (with 45 min of Ar purging before adding powders). The mixture was transferred into the 50-ml autoclave, maintained at 210 °C for 90 min. The product collected, known as BTO NWs, was carefully washed and then dried at 80 °C.

KNO NWs were synthesized following a reported hydrothermal procedure.[32] First, 12.63 g KOH was dissolved in 15 ml deionized water. Then, 0.87 g of Nb powder was dispersed into the KOH solution by sonication for 2h. The mixture was then transferred into a 25-ml Teflon-lined stainless autoclave and maintained at 140 °C for 15h under 600 rpm stirring. A white product containing NWs and sub-micro particles was collected and carefully washed. About 0.2 g of mostly NWs were obtained from the product by centrifugation and subsequently dried at 80 °C.

Composite formulation. Composites of the nanomaterials were formulated with polyvinyl alcohol (PVA) matrices by a solution casting method. First, a desired weight of NWs was added into DI water and sonicated for 30 minutes. Then 1.20 g of PVA 15 wt.% aqueous solution (by dissolving PVA pellets in water at 95 °C under stirring for 4 h) was added to the nanowire/water mixture. The mixture is then stirred for 4h to achieve a homogeneous dispersion of the NWs in the PVA solution. After degassing, the solution was cast on a PMMA substrate by doctor blading. The films were immediately dried at 75 °C to solidify the PVA matrix. Finally, the films detached from the substrate were dried at 100 °C under vacuum overnight. The composite films have a thickness below 100 μm. Aside from the synthesized NWs, commercial BTO NPs of 100 and 500 nm in size (labeled as BTO100 and BTO500, respectively) were employed for control composites.

Morphology and structure characterizations. The morphology and the crystalline structure of the NWs and the composites were characterized by scanning electron microscopy (SEM, Hitachi

TM1000, and S4500), transmission electron microscopy (TEM, 1400 JEOL operating at 120 kV), X-ray diffraction (XRD, PANalytical Empyrean diffractometer, using a Cu Kα source λ= 0.15418 nm) and Raman spectroscopy (XploRA Horiba Jobin Yvon, using a 532-nm laser).

Electrical measurements. For electrical characterizations, the composites were metalized on both sides to form capacitors with circular Au electrodes of 9.0 mm in diameter by a vacuum sputter. The dielectric constant and AC conductivity of the composites were measured as a function of frequency from 10^{-1} to 10^{6} Hz by an impedance analyzer (MaterialsMates 7260). Electrical poling across the film thickness was performed by a contact mode in silicone oil under a DC voltage (Trek, USA). The capacitor was first heated to a desired temperature then the poling voltage was applied for 1h. The heating was then turned off and the capacitor was cooled down under the voltage for 30 min. After the poling, the capacitor was short-circuited to release trapped charges and then aged for at least 24 hours to release internal stress induced by the poling. Piezoelectric coefficient d_{33} (pC/N) was then measured (in the direction across the film thickness) by a PM-200 piezometer (Piezotest, UK), with a dynamic force of 0.25 N at a standard frequency of 110 Hz. The poling temperature and poling field were varied to study the poling characteristics of the composites. For each composite, at least two capacitors were studied at every poling condition to obtain the standard mean and deviation of the d_{33} coefficient.

Second harmonic measurements. Second harmonic generation (SHG) microscopy mapping was conducted over non-poled single NWs embedded in a PVA matrix using a 120-fs pulsed laser with a 76-MHz repetition rate and an excitation wavelength of 800 nm (Coherent Mira 900f). The SHG was detected at 400 nm. Polarization and power were controlled using a series of polarizers and half-wave plates. The laser was focused on the sample using a ×100 microscope objective (N.A. = 0.95). A piezoelectric stage was used to raster scan the sample along the X and Y directions with a

step size of 50 nm and an acquisition time of 20 ms for each point. For the mapping experiments, the polarization of the incident light was set horizontally (X-direction). The polarized SHG maps were collected simultaneously along the horizontal (X) and vertical (Y) directions using two single-photon avalanche photodiodes operating in photon counting mode. The resulting SHG maps are the sum of the two polarized maps (X+Y). Polar plots were collected on selected points over the NWs. In these experiments, the input polarization was varied over a period (360°) and the signal was collected every 10° on the two channels with orthogonal analyzers.[53] For each orientation of the input polarizer, the signal was integrated over 20 ms.

ASSOCIATED CONTENT

Supporting Information. Additional data and figures are included in the Supplementary Information. **Figure S1**. Piezoelectric coefficient d_{33} of BTO, KNO, and NNO bulk ceramics reported in the literature. The deviations were calculated from the maximum and minimum values reported in each study. **Figure S2.** Raman spectra of NNO NWs and NNO NPs. It is seen that the Raman peaks of NNO NWs are consistent with those of NNO ferroelectric phase while the Raman peaks of NNO NPs are consistent with those of NNO anti-ferroelectric phase. **Figure S3.** (a-b) SEM images of BTO NWs. (c) Raman spectra of BTO NWs, BTO100, and BTO500 NPs. (d) XRD patterns of BTO materials measured at room temperature. Peaks are indexed to the diffractions of a BTO tetragonal structure (ICSD 98-001-5453). (e) Enlarged XRD patterns around $2\theta = 45.2°$ of BTO materials measured *in situ* at room temperature and 150 ºC. **Figure S4.** (a-b) SEM images and (c) Overall XRD pattern of KNO NWs. (d) Enlarged XRD pattern of KNO NWs at $2\theta \approx 45.2°$ fitted by triple peaks of a monoclinic structure. **Figure S5.** AC conductivity of the PVA/BTO500-50 wt.% composite at various temperatures. **Figure S6.** (a-c) Dielectric constant of PVA/NW

nanocomposites. (d) Dielectric loss of NW-50 wt.% nanocomposites. The dielectric constants at 10^3 Hz were used to calculate the piezoelectric FOM of the nanocomposites. **Table S1.** Some piezoelectric composites of tetragonal BTO NPs reported in the literature. "This material is available free of charge via the Internet at http://pubs.acs.org."

AUTHOR INFORMATION

Corresponding Author

Poulin P., Centre de Recherche Paul Pascal, University of Bordeaux, CNRS, Pessac 33600, France

Email: philippe.poulin@crpp.cnrs.fr

ACKNOWLEDGMENTS

This study received financial support from the French government in the framework of the University of Bordeaux's Bordeaux's France 2030 program/GPR PPM and from the ANR POETICS project ANR-17-CE05-0004-01. CL and FLL acknowledge the support of the Natural Sciences and Engineering Research Council (NSERC) of Canada through a Discovery Grant (DGRGPIN-2020-06676). The authors acknowledge F. Weill for his support in TEM measurements.

Author contributions

Conceptualization: P.P., M.H.D., M.M., A.C. Nanowire synthesis: M.T.D., K.Z., A.S.D., R.M. Nanowire characterizations: M.T.D., E.L. SHG measurements: C.L., F.L.L. Composite formation

and characterization: M.T.D., J.Y., W.N. Writing - original draft: M.T.D., P.P., M.H.D. Writing - review & editing: M.T.D., P.P., M.H.D. All authors have discussed the results and contributed to the final manuscript.

Conflicts of interest

There are no conflicts to declare.

REFERENCES

(1) Newnham, R. E.; Bowen, L. J.; Klicker, K. A.; Cross, L. E. Composite Piezoelectric Transducers. *Materials & Design* **1980**, *2* (2), 93–106.

(2) Akdogan, E. K.; Allahverdi, M.; Safari, A. Piezoelectric Composites for Sensor and Actuator Applications. *IEEE Trans. Ultrason. Ferroelectr. Freq. Control* **2005**, *52* (5), 746–775.

(3) Hu, D.; Yao, M.; Fan, Y.; Ma, C.; Fan, M.; Liu, M. Strategies to Achieve High Performance Piezoelectric Nanogenerators. *Nano Energy* **2019**, *55*, 288–304.

(4) Andrews, C.; Lin, Y.; Sodano, H. A. The Effect of Particle Aspect Ratio on the Electroelastic Properties of Piezoelectric Nanocomposites. *Smart Mater. Struct.* **2010**, *19* (2), 025018.

(5) Andrews, C.; Lin, Y.; Tang, H.; Sodano, H. A. Influence of Aspect Ratio on Effective Electromechanical Coupling of Nanocomposites with Lead Zirconate Titanate Nanowire Inclusion. *J. Intell. Mater. Syst. Struct.* **2011**, *22* (16), 1879–1886.

(6) Zhou, Z.; Bowland, C. C.; Malakooti, M. H.; Tang, H.; Sodano, H. A. Lead-Free $0.5Ba(Zr_{0.2}Ti_{0.8})O_3–0.5(Ba_{0.7}Ca_{0.3})TiO_3$ Nanowires for Energy Harvesting. *Nanoscale* **2016**, *8* (9), 5098–5105.

(7) Nafari, A.; Sodano, H. A. Electromechanical Modeling and Experimental Verification of a Direct Write Nanocomposite. *Smart Mater. Struct.* **2019**, *28* (4), 045014.

(8) Nafari, A.; Sodano, H. A. Tailored Nanocomposite Energy Harvesters with High Piezoelectric Voltage Coefficient through Controlled Nanowire Dispersion. *Nano Energy* **2019**, *60*, 620–629.

(9) Tu, R.; Zhang, B.; Sodano, H. A. Lead Titanate Nanowires/Polyamide-Imide Piezoelectric Nanocomposites for High-Temperature Energy Harvesting. *Nano Energy* **2022**, *97*, 107175.

(10) Nairn, J. A. On the Use of Shear-Lag Methods for Analysis of Stress Transfer in Unidirectional Composites. *Mechanics of Materials* **1997**, *26* (2), 63–80.

(11) Young, R. J. Composite Micromechanics. In *Structural Integrity and Durability of Advanced Composites*; Elsevier, 2015; pp 3–23.

(12) Zhong, W. L.; Wang, Y. G.; Zhang, P. L.; Qu, B. D. Phenomenological Study of the Size Effect on Phase Transitions in Ferroelectric Particles. *Phys. Rev. B* **1994**, *50* (2), 698–703.

(13) Jiang, B.; Peng, J. L.; Bursill, L. A.; Zhong, W. L. Size Effects on Ferroelectricity of Ultrafine Particles of $PbTiO_3$. *J. Appl. Phys.* **2000**, *87* (7), 3462–3467.

(14) Hoshina, T. Size Effect of Barium Titanate: Fine Particles and Ceramics. *J. Ceram. Soc. Japan* **2013**, *121* (1410), 156–161.

(15) Shiratori, Y.; Magrez, A.; Dornseiffer, J.; Haegel, F.-H.; Pithan, C.; Waser, R. Polymorphism in Micro-, Submicro-, and Nanocrystalline $NaNbO_3$. *J. Phys. Chem. B* **2005**, *109* (43), 20122–20130.

(16) Koruza, J.; Tellier, J.; Malič, B.; Bobnar, V.; Kosec, M. Phase Transitions of Sodium Niobate Powder and Ceramics, Prepared by Solid State Synthesis. *J. Appl. Phys.* **2010**, *108* (11), 113509.

(17) Zhu, H.; Zheng, Z.; Gao, X.; Huang, Y.; Yan, Z.; Zou, J.; Yin, H.; Zou, Q.; Kable, S. H.; Zhao, J.; Xi, Y.; Martens, W. N.; Frost, R. L. Structural Evolution in a Hydrothermal Reaction between Nb_2O_5 and NaOH Solution: From Nb_2O_5 Grains to Microporous $Na_2Nb_2O_6 \cdot {}^2/_3H_2O$ Fibers and $NaNbO_3$ Cubes. *J. Am. Chem. Soc.* **2006**, *128* (7), 2373–2384.

(18) Ke, T.-Y.; Chen, H.-A.; Sheu, H.-S.; Yeh, J.-W.; Lin, H.-N.; Lee, C.-Y.; Chiu, H.-T. Sodium Niobate Nanowire and Its Piezoelectricity. *J. Phys. Chem. C* **2008**, *112* (24), 8827–8831.

(19) David, C.; Capsal, J.-F.; Laffont, L.; Dantras, E.; Lacabanne, C. Piezoelectric Properties of Polyamide 11/$NaNbO_3$ Nanowire Composites. *J. Phys. D: Appl. Phys.* **2012**, *45* (41), 415305.

(20) Jung, J. H.; Lee, M.; Hong, J.-I.; Ding, Y.; Chen, C.-Y.; Chou, L.-J.; Wang, Z. L. Lead-Free $NaNbO_3$ Nanowires for a High Output Piezoelectric Nanogenerator. *ACS Nano* **2011**, *5* (12), 10041–10046.

(21) Ji, S.; Liu, H.; Sang, Y.; Liu, W.; Yu, G.; Leng, Y. Synthesis, Structure, and Piezoelectric Properties of Ferroelectric and Antiferroelectric $NaNbO_3$ Nanostructures. *CrystEngComm* **2014**, *16* (32), 7598–7604.

(22) Liu, Z.; Ji, M.; Yang, Q.; Zhang, Y.; Hu, Y.; He, Y.; Li, B.; Wang, J. Silicone-Oil-Assisted Synthesis of High-Quality Sodium Niobate Nanowires. *CrystEngComm* **2017**, *19* (26), 3553–3556.

(23) Chen, J.; Feng, D. TEM Study of Phases and Domains in $NaNbO_3$ at Room Temperature. *Phys. Stat. Sol. (a)* **1988**, *109* (1), 171–185.

(24) Gao, L.; Guo, H.; Zhang, S.; Randall, C. A. Stabilized Antiferroelectricity in $xBiScO_3$-(1-x)$NaNbO_3$ Lead-Free Ceramics with Established Double Hysteresis Loops. *Applied Physics Letters* **2018**, *112* (9), 092905.

(25) Koruza, J.; Groszewicz, P.; Breitzke, H.; Buntkowsky, G.; Rojac, T.; Malič, B. Grain-Size-Induced Ferroelectricity in $NaNbO_3$. *Acta Mater.* **2017**, *126*, 77–85.

(26) Tyunina, M.; Levoska, J. Unstable State in Epitaxial Films of Sodium Niobate. *Applied Physics Letters* **2009**, *95* (10), 102903.

(27) Yuzyuk, Yu. I.; Shakhovoy, R. A.; Raevskaya, S. I.; Raevski, I. P.; El Marssi, M.; Karkut, M. G.; Simon, P. Ferroelectric Q-Phase in a $NaNbO_3$ Epitaxial Thin Film. *Appl. Phys. Lett.* **2010**, *96* (22), 222904.

(28) Schwarzkopf, J.; Schmidbauer, M.; Remmele, T.; Duk, A.; Kwasniewski, A.; Bin Anooz, S.; Devi, A.; Fornari, R. Strain-Induced Phase Transitions in Epitaxial $NaNbO_3$ Thin Films Grown by Metal–Organic Chemical Vapour Deposition. *J Appl Crystallogr* **2012**, *45* (5), 1015–1023.

(29) Seol, D.; Kim, B.; Kim, Y. Non-Piezoelectric Effects in Piezoresponse Force Microscopy. *Current Applied Physics* **2017**, *17* (5), 661–674.

(30) Bao, N.; Shen, L.; Srinivasan, G.; Yanagisawa, K.; Gupta, A. Shape-Controlled Monocrystalline Ferroelectric Barium Titanate Nanostructures: From Nanotubes and Nanowires to Ordered Nanostructures. *J. Phys. Chem. C* **2008**, *112* (23), 8634–8642.

(31) Surmenev, R. A.; Chernozem, R. V.; Skirtach, A. G.; Bekareva, A. S.; Leonova, L. A.; Mathur, S.; Ivanov, Yu. F.; Surmeneva, M. A. Hydrothermal Synthesis of Barium Titanate Nano/Microrods and Particle Agglomerates Using a Sodium Titanate Precursor. *Ceram. Int.* **2021**, *47* (7), 8904–8914.

(32) Kim, S.; Lee, J.-H.; Lee, J.; Kim, S.-W.; Kim, M. H.; Park, S.; Chung, H.; Kim, Y.-I.; Kim, W. Synthesis of Monoclinic Potassium Niobate Nanowires That Are Stable at Room Temperature. *J. Am. Chem. Soc.* **2013**, *135* (1), 6–9.

(33) Sa-Gong, G.; Safari, A.; Jang, S. J.; Newnham, R. E. Poling Flexible Piezoelectric Composites. *Ferroelectr. Lett. Sect.* **1986**, *5* (5), 131–142.

(34) Furukawa, T.; Suzuki, K.; Date, M. Switching Process in Composite Systems of PZT Ceramics and Polymers. *Ferroelectrics* **1986**, *68* (1), 33–44.

(35) Egginger, M.; Irimia-Vladu, M.; Schwödiauer, R.; Tanda, A.; Frischauf, I.; Bauer, S.; Sariciftci, N. S. Mobile Ionic Impurities in Poly(Vinyl Alcohol) Gate Dielectric: Possible Source of the Hysteresis in Organic Field-Effect Transistors. *Adv. Mater.* **2008**, *20* (5), 1018–1022.

(36) Capsal, J.-F.; David, C.; Dantras, E.; Lacabanne, C. Piezoelectric Sensing Coating for Real-Time Impact Detection and Location on Aircraft Structures. *Smart Mater. Struct.* **2012**, *21* (5), 055021.

(37) Ge, H.; Hou, Y.; Zhu, M.; Wang, H.; Yan, H. Facile Synthesis and High d_{33} of Single-Crystalline $KNbO_3$ Nanocubes. *Chem. Commun.* **2008**, No. 41, 5137.

(38) Kakimoto, K.; Ito, T.; Ohsato, H. Synthesis of $KNbO_3$ Piezoelectric Ceramics Using Citrate Precursors. *Jpn. J. Appl. Phys.* **2008**, *47* (9), 7669–7672.

(39) Ge, H.; Hou, Y.; Wang, C.; Zhu, M.; Yan, H. Synthesis and Piezoelectric Properties of $KNbO_3$ Ceramics by Molten-Salt Synthetic Method. *Jpn. J. Appl. Phys.* **2009**, *48* (4), 041405.

(40) Ge, H.; Hou, Y.; Rao, X.; Zhu, M.; Wang, H.; Yan, H. The Investigation of Depoling Mechanism of Densified $KNbO_3$ Piezoelectric Ceramic. *Appl. Phys. Lett.* **2011**, *99* (3), 032905.

(41) Ge, H.; Hou, Y.; Xia, C.; Zhu, M.; Wang, H.; Yan, H. Preparation and Piezoelectricity of $NaNbO_3$ High-Density Ceramics by Molten Salt Synthesis. *J. Am. Ceram. Soc.* **2011**, *94* (12), 4329–4334.

(42) Chao, L.; Hou, Y.; Zheng, M.; Yue, Y.; Zhu, M. Macroscopic Ferroelectricity and Piezoelectricity in Nanostructured $NaNbO_3$ Ceramics. *Appl. Phys. Lett.* **2017**, *110* (12), 122901.

(43) Huan, Y.; Wang, X.; Fang, J.; Li, L. Grain Size Effect on Piezoelectric and Ferroelectric Properties of $BaTiO_3$ Ceramics. *J. Eur. Ceram.* **2014**, *34* (5), 1445–1448.

(44) Tan, Y.; Zhang, J.; Wu, Y.; Wang, C.; Koval, V.; Shi, B.; Ye, H.; McKinnon, R.; Viola, G.; Yan, H. Unfolding Grain Size Effects in Barium Titanate Ferroelectric Ceramics. *Sci. Rep.* **2015**, *5* (1), 9953.

(45) Qi, F.; Chen, N.; Wang, Q. Dielectric and Piezoelectric Properties in Selective Laser Sintered Polyamide11/$BaTiO_3$/CNT Ternary Nanocomposites. *Materials & Design* **2018**, *143*, 72–80.

(46) Zhang, M.-H.; Fulanović, L.; Egert, S.; Ding, H.; Groszewicz, P. B.; Kleebe, H.-J.; Molina-Luna, L.; Koruza, J. Electric-Field-Induced Antiferroelectric to Ferroelectric Phase Transition in Polycrystalline $NaNbO_3$. *Acta Mater.* **2020**, *200*, 127–135.

(47) Park, K.-I.; Bae, S. B.; Yang, S. H.; Lee, H. I.; Lee, K.; Lee, S. J. Lead-Free $BaTiO_3$ Nanowires-Based Flexible Nanocomposite Generator. *Nanoscale* **2014**, *6* (15), 8962.

(48) Jeong, C. K.; Baek, C.; Kingon, A. I.; Park, K.; Kim, S. Lead-Free Perovskite Nanowire-Employed Piezopolymer for Highly Efficient Flexible Nanocomposite Energy Harvester. *Small* **2018**, *14* (19), 1704022.

(49) Xie, B.; Zhang, H.; Zhang, Q.; Zang, J.; Yang, C.; Wang, Q.; Li, M.-Y.; Jiang, S. Enhanced Energy Density of Polymer Nanocomposites at a Low Electric Field through Aligned $BaTiO_3$ Nanowires. *J. Mater. Chem. A* **2017**, *5* (13), 6070–6078.

(50) Shen, Y. R. *Principles of Nonlinear Optics*, Wiley Classics Library ed.; Wiley Classics Library; Wiley-Interscience: Hoboken, NJ, 2003.

(51) Bihari, B.; Kumar, J.; Stauf, G. T.; Van Buskirk, P. C.; Hwang, C. S. Investigation of Barium Titanate Thin Films on MgO Substrates by Second-harmonic Generation. *J. Appl. Phys.* **1994**, *76* (2), 1169–1174.

(52) Xu, R.; Crust, K. J.; Harbola, V.; Arras, R.; Patel, K. Y.; Prosandeev, S.; Cao, H.; Shao, Y.; Behera, P.; Caretta, L.; Kim, W. J.; Khandelwal, A.; Acharya, M.; Wang, M. M.; Liu, Y.; Barnard, E. S.; Raja, A.; Martin, L. W.; Gu, X. W.; Zhou, H.; Ramesh, R.; Muller, D. A.; Bellaiche, L.; Hwang, H. Y. Size-Induced Ferroelectricity in Antiferroelectric Oxide Membranes. *Adv. Mater.* **2023**, *35* (17), 2210562.

(53) McRae, D. M.; Therien, D. A. B.; Hou, R.; Wallace, G. Q.; Lagugné-Labarthet, F. Sierpiński Fractals as Plasmonic Metastructures for Second-Harmonic Generation. *ACS Appl. Nano Mater.* **2020**, *3* (4), 3922–3929.

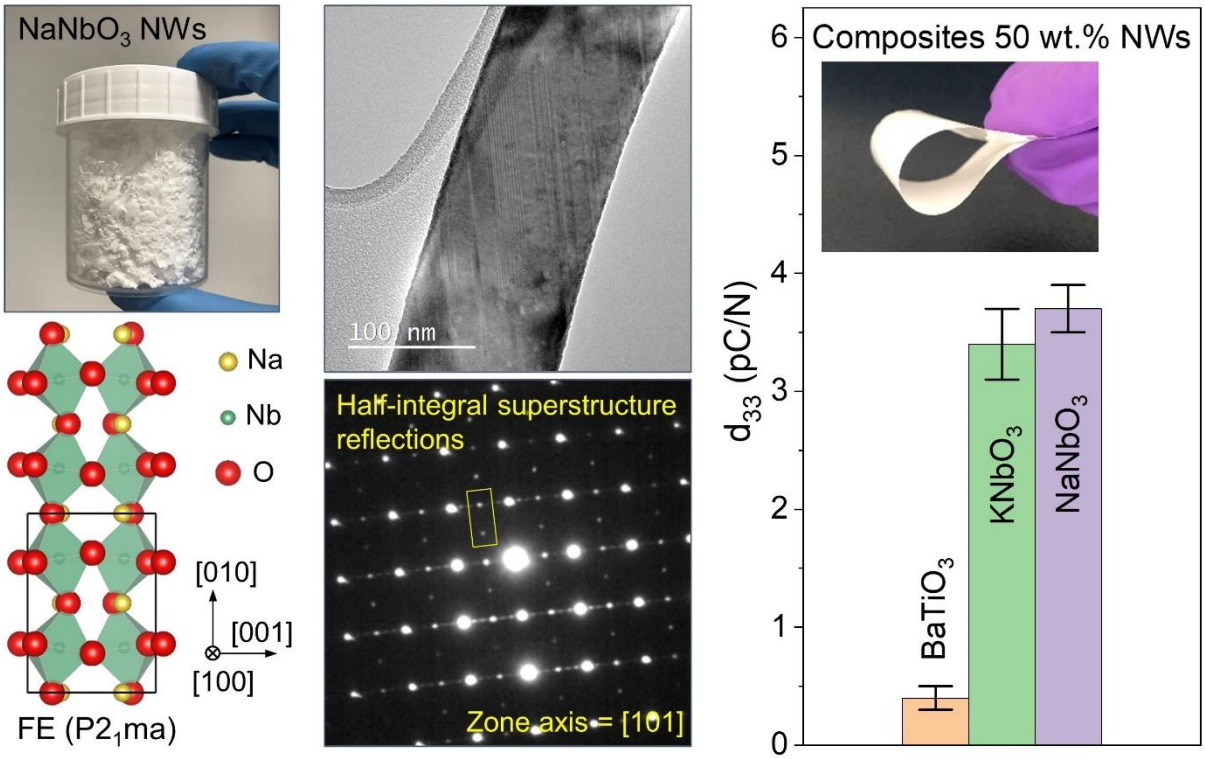

Graphic abstract: (Top-left) Photograph of $NaNbO_3$ NWs obtained by one hydrothermal synthesis in a 200-ml autoclave. (Bottom-left) Schematic crystal structures of $NaNbO_3$ ferroelectric (FE) phase. (Top-middle) Transmission electron microscopy images showing strip patterns of ferroelectric domains inside a $NaNbO_3$ NW. (Bottom-middle) The corresponding electron diffraction with half-integral superstructure reflections of the FE-phase $NaNbO_3$ NWs. (Right) The superior piezoelectric performance of $NaNbO_3$ NWs compared to $BaTiO_3$ NWs. The inset shows the photograph of a nanocomposite film with 50 wt.% $NaNbO_3$ NWs.